

Constraining Dike Opening Models With Seismic Velocity Changes Associated With the 2023–2024 Eruption Sequence on the Reykjanes Peninsula

E. Bird¹, J. Atterholt^{1,2}, J. Li¹, E. Biondi¹, Q. Zhai¹, L. Li¹, Y. Yang^{1,3}, J. Fang¹, X. Wei¹, V. Hjörleifsdóttir⁴, A. Klesh⁵, V. Kamalov⁶, T. Gunnarsson⁷, and Z. Zhan¹

¹California Institute of Technology, Pasadena, CA, USA, ²Now at: Geological Hazards Science Center, Golden, CO, USA, ³Now at: Scripps Institute of Oceanography, San Diego, CA, USA, ⁴Reykjavik University, Reykjavik, Iceland, ⁵Jet Propulsion Laboratory, Pasadena, CA, USA, ⁶Valey Kamalov LLC, Gainesville, FL, USA, ⁷Google, Mountain View, CA, USA

Peer Review The peer review history for this article is available as a PDF in the Supporting Information.

Key Points:

- Subsurface deformation associated with the 2023–2024 eruption sequence on the Reykjanes Peninsula produces a pronounced dv/v signal
- The observed dv/v signal is inverted for a model of dike-opening which agrees with surface fissure locations
- This result demonstrates that inversion of stress-induced dv/v signals is viable

Supporting Information:

Supporting Information may be found in the online version of this article.

Correspondence to:

E. Bird,
elijahjosephbird@gmail.com

Citation:

Bird, E., Atterholt, J., Li, J., Biondi, E., Zhai, Q., Li, L., et al. (2025). Constraining dike opening models with seismic velocity changes associated with the 2023–2024 eruption sequence on the Reykjanes Peninsula. *AGU Advances*, 6, e2024AV001516. <https://doi.org/10.1029/2024AV001516>

Received 30 SEP 2024

Accepted 3 FEB 2025

Author Contributions:

Conceptualization: Z. Zhan

Data curation: V. Hjörleifsdóttir

Formal analysis: Q. Zhai

Funding acquisition: Z. Zhan

Investigation: E. Bird

Methodology: E. Bird, J. Atterholt,

E. Biondi, L. Li, Z. Zhan

Project administration: Z. Zhan

Resources: V. Hjörleifsdóttir, A. Klesh,

V. Kamalov, T. Gunnarsson

Software: Y. Yang

Supervision: J. Atterholt, E. Biondi,

Z. Zhan

© 2025. The Author(s).

This is an open access article under the terms of the [Creative Commons Attribution-NonCommercial-NoDerivs](#)

License, which permits use and

distribution in any medium, provided the

original work is properly cited, the use is

non-commercial and no modifications or

adaptations are made.

Abstract The stress field perturbation caused by magmatic intrusions within volcanic systems induces strain in the surrounding region. This effect results in the opening and closing of microcracks in the vicinity of the intrusion, which can affect regional seismic velocities. In late November 2023, we deployed a distributed acoustic sensing interrogator to convert an existing 100-km telecommunication fiber-optic cable along the coast of Iceland's Reykjanes peninsula into a dense seismic array, which has run continuously. Measuring changes in surface wave moveout with ambient noise cross-correlation, we observe up to 2% changes in Rayleigh wave phase velocity (dv/v) following eruptions in the peninsula's 2023–2024 sequence that are likely associated with magmatic intrusions into the eruption-feeding dike. We apply a Bayesian inversion to compute the posterior distribution of potential dike opening models for each eruption by considering dv/v measurements for varying channel pairs and frequency bands, and assuming this velocity change is tied to volumetric strain associated with dike-opening. Our results are in agreement with those based on geodetic measurement and provide independent constraints on the depth of the dike, demonstrating the viability of this novel inversion and new volcano monitoring directions through fiber sensing.

Plain Language Summary In volcanic regions, pressure from intruding magma can cause nearby rocks to deform. The speed of seismic waves through said rocks then increases or decreases, as the medium stretches and compresses. Prior to the 2023–2024 eruption sequence on the Reykjanes peninsula, we deployed an interferometric instrument which converted an existing optical fiber into an array of ground-motion sensors. With our array, we see a significant change in seismic velocities following eruptions, as the magma feeding the eruption moves through the subsurface. Through observation of the seismic velocity change in each eruption, we can better understand the subsurface structure of the volcanic system. We constrain the location, azimuth, length, and depth of the intruding dike using only these changes in the seismic velocity. Our constraints may be considered in tandem with those derived geodetically to better understand the dike structure.

1. Introduction

Located at the intersection of a mantle hotspot and the mid-atlantic ridge, Iceland is a vigorously volcanic region. In recent years, Iceland's Reykjanes peninsula (Figure 1) entered a period of activity, with its most recent eruptive series beginning in late 2023 and continuing to present (Parks et al., 2024). On 10 November 2023, a dike formed in the subsurface of the Reykjanes peninsula, striking approximately northeast (Sigmundsson et al., 2024). The intrusion was followed by a series of volcanic eruptions, the first of which occurred from December 18–21, 2023. This work studies the behavior of the volcanic system through observed changes in seismic velocities on the peninsula during the first three eruptions in the sequence.

Temporal variations in seismic velocities (dv/v) may be indicative of myriad earth processes. Changes in the water saturation of a rock can affect its seismic velocities, so dv/v can act as an indirect measure of groundwater levels and the broad hydrological state of the subsurface (Clements & Denolle, 2018; Rodríguez Tribaldos & Ajo-Franklin, 2021; Sens-Schönfelder & Wegler, 2006; Shen et al., 2024). Changes in the microcrack density in a material can likewise impact velocities, so a velocity change may indicate volumetric strain in certain contexts. This effect makes dv/v a powerful metric in studies of the coseismic and postseismic stress and strain fields

Validation: J. Li
 Visualization: E. Bird
 Writing – original draft: E. Bird
 Writing – review & editing: E. Bird,
 J. Atterholt, J. Li, E. Biondi, Q. Zhai, L. Li,
 J. Fang, X. Wei, V. Kamalov, Z. Zhan

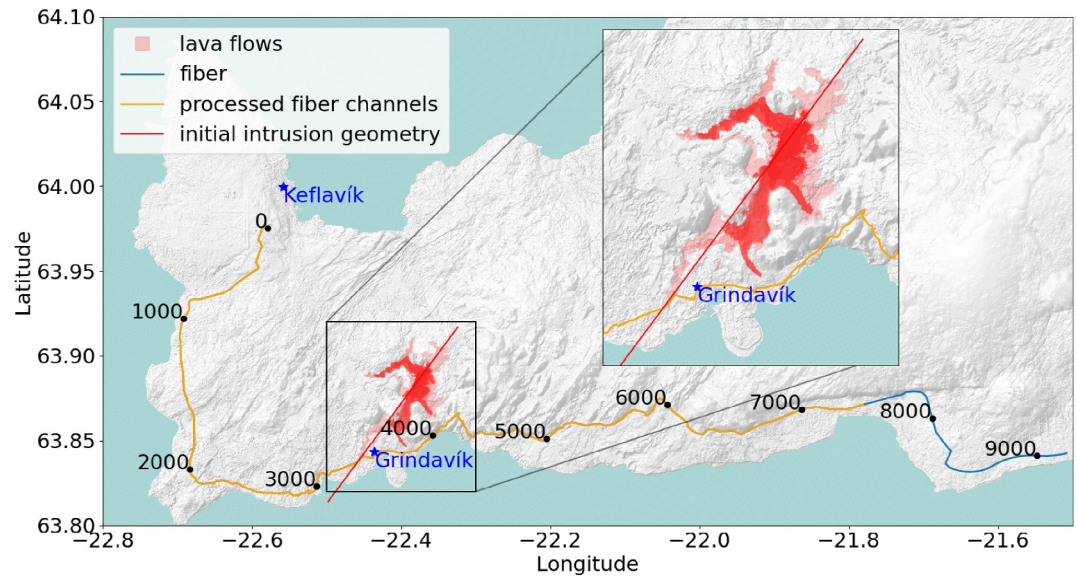


Figure 1. Map of the Reykjanes Peninsula, with fiber channels and lava flow outlines plotted (LMI, 2024). Lava flows are darker in locations where lava flows from multiple eruptions overlap. Channel numbers are listed at 1000 channel intervals after removal of bad channels. The geometry of the initial intrusion from Sigmundsson et al. (2024) is plotted in red.

associated with large earthquakes (Wegler & Sens-Schönfelder, 2007; Çubuk-Sabuncu et al., 2024). Similarly, dv/v signals can provide insights into the magmatic structures feeding volcanic systems, which will strain surrounding bodies of rock (Brennguier et al., 2008; Donaldson et al., 2017; Mordret et al., 2010; Sens-Schönfelder et al., 2014). While such volcanic signals may produce significant velocity changes, competing environmental signals may complicate interpretations (e.g., Donaldson et al. (2019)). Generally, studies of dv/v in volcanic regions consider how surface wave phase velocity perturbations in one or more frequency bands respond to observed volcanic events, sometimes comparing these perturbations with volumetric strains estimated through geodetic measurements or modeled with point sources (Donaldson et al., 2019; Kiyoo, 1958; Maass et al., 2024; Mordret et al., 2010).

Many studies calculate dv/v signals on the basis of ambient noise cross-correlation, a method wherein continuous data from two seismic sensors are cross-correlated over a sufficiently long time window, yielding an approximation to the Green's function between the two sensors (Campillo & Paul, 2003). Relying on ambient noise, one can produce continuous estimates of the seismic velocity, a benefit over estimates of velocity changes which rely on repetitive sources (Sens-Schönfelder & Wegler, 2006). However, results are highly sensitive to changes in the noise source over time, with past results near our study site indicating sensitivity of low-frequency dv/v to ocean dynamics (Zhan et al., 2013; Çubuk-Sabuncu et al., 2024).

The core data set in this study is derived from a fiber-optic seismic array (Zhan, 2020). Fiber-optic seismic arrays consist of an interrogator unit (IU), attached to an optical fiber. The IU transmits a laser signal into the fiber and records backscattered light from impurities in the fiber. As the fiber strains, the delay between subsequent backscattered arrivals at the interrogator will change. Applying interferometric techniques to this changing backscatter signal, one can extract the strain of the fiber over time at meter-scale intervals. Fiber-optic seismology is an efficient method of densely instrumenting a large region with seismic sensors, as researchers can interrogate unused fibers in existing telecommunication networks. Fiber-optic seismology has been successfully utilized in wide-ranging geophysical fields including seismic imaging (e.g., Ajo-Franklin et al., 2019; Atterholt et al., 2024; Cheng et al., 2023; Ma et al., 2023; Martuganova et al., 2022; Yang et al., 2022), seismicity (e.g., Ajo-Franklin et al., 2019; J. Li et al., 2023), hydrology (e.g., Rodríguez Tribaldos & Ajo-Franklin, 2021; Shen et al., 2024), and physical oceanography (e.g., Lindsey et al., 2019; Mata Flores et al., 2023; Sladen et al., 2019; Williams et al., 2019, 2023). In the field of volcanology, numerous studies have leveraged the spatial density of fiber-optic arrays in characterizing the structure and dynamics of volcanic systems (Biondi et al., 2023; Caudron et al., 2024; Jousset et al., 2022; Klaasen et al., 2023). One recent study of volcanic dv/v employed data from a fiber-optic

array, demonstrating improved correlations when data were spatially averaged over the dense array (Maass et al., 2024).

2. Data

On 20 November 2023, we deployed an Optasense QuantX Interrogator Unit at a fiber node in Keflavík, Iceland, converting a 102 km fiber to a dense set of strainmeters. The fiber runs south from Keflavík to the southwest corner of the Reykjanes peninsula, and continues eastward along the coast, passing through Grindavík. Data are recorded at a sampling rate of 160 Hz with a gauge length of 100 and 10 m channel spacing. The deployment concluded in November 2024.

We determine the location of fiber channels as in Biondi et al. (2022). This procedure first distinguishes bad channels and fiber loops, sections of cable which are largely uncoupled with the surrounding earth structure and provide little useful geophysical data. Based on recordings of local seismic events, we identify 986 of the initial 10,200 fiber channels as bad channels. To localize the remaining channels, we drive across the array in a GPS-equipped vehicle. Station numbers (after removal of bad channels) are plotted at 1,000 channel (10 km) intervals in Figure 1.

The data are processed to produce ambient noise cross-correlation empirical Green's functions (EGFs), calculated for each day of the study period. To produce these EGFs, we filter data between 0.05 and 10 Hz, downsample to 20 Hz, perform temporal normalization, and spectrally whiten between 0.05 and 10 Hz, as in Yang et al. (2022).

3. Analysis

3.1. Extracting dv/v Estimates

We extract dv/v estimates from our data using the stretching method (an established method which is detailed in Text S1 in Supporting Information S1). To implement this approach, we must choose a time window of the EGF to stretch over. We intend to capture the change in direct arrival time for a given channel pair. Thus, we predict a direct arrival time t_{arr} from the velocity model described in Málek et al. (2019) and select a window around the predicted arrival spanning (t_{min}, t_{max}) , where $t_{min} = \frac{2}{3}t_{arr}$ and $t_{max} = \max(2t_{arr}, t_{min} + 8)$. We require a minimum length of 8 s for each window to ensure a stable solution. While our relatively long time windows will cover a portion of the EGF coda, a high amplitude direct arrival will generally dominate the result.

We first perform an approximate constant offset dv/v analysis, considering daily cross-correlations of channel pairs separated by 500 channels (approximately 5 km), band-passed near 1.0 s. These estimates of dv/v are calculated relative to a stacked EGF over the first 100 days of the study. We find that the data set is dominated by a change in seismic velocity following each eruption (Figure 2). Thus, the core analysis of this work considers only dv/v signals associated with the eruptions, with cross-correlations summed over the full inter-eruption periods to produce the differential measurement. We only consider the first three eruptions, as the following eruptions see intense volcanic noise biasing our results. Text S2 and Figure S1 in Supporting Information S1 detail the data quality control employed in producing our dv/v estimates.

Our inversion is based on pairwise dt/t estimates for periods T of 0.5, 1.0, and 2.0 s, for starting channels p_{init} ranging from 0 to 6,000 at 10 channel intervals, and for ending channels q_{init} from $p_{init} + 200$ to $p_{init} + 1300$ at 10 channel intervals. This choice limits inter-channel offsets to at most ≈ 13 km, as our dv/v estimates become significantly noisier at increased displacements, especially in the higher frequency bands.

We smooth and downsample our data for each eruption, arriving at data points, $\left(\frac{dt}{t}\right)_{pqT}$, where:

$$\left(\frac{dt}{t}\right)_{pqT} = \frac{1}{25} \sum_{r=0}^4 \sum_{s=0}^4 \left(\frac{dt}{t}\right)_{(p_{init}=p+(10r))(q_{init}=q+(10s))T}, \quad (1)$$

where $p \in \{0, 100, \dots, 5800, 5900\}$, $q \in \{p + 200, p + 350, \dots, p + 1100, p + 1250\}$, and $T \in \{0.5, 1.0, 2.0\}$. Taking the standard deviation across these channel pairs, rather than the mean, we can also produce an uncertainty estimate for each of our smoothed data points. Data and uncertainty for all eruptions and frequency bands discussed are plotted in Supplementary Figures S2–S4 in Supporting Information S1.

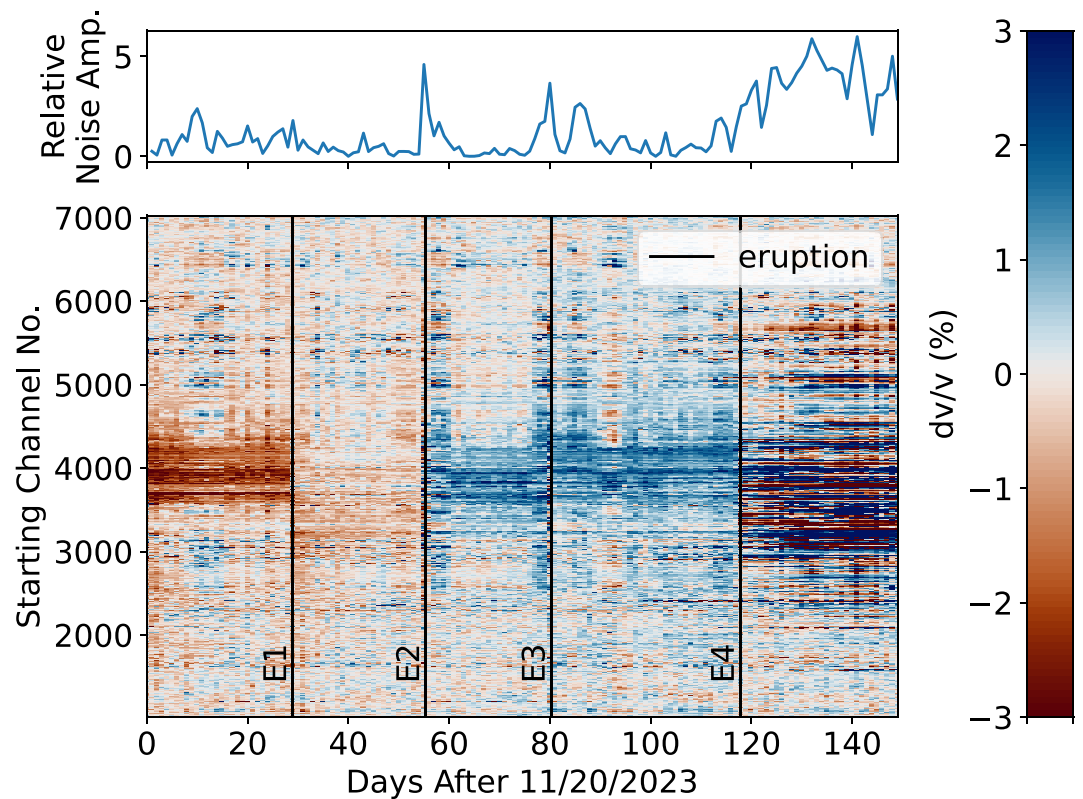


Figure 2. The colormap shows dv/v across the first 150 days of our deployment, calculated at 1.0 Hz with channel pairs separated by 500 channels (approximately 5 km). The dates of the eruptions are denoted by vertical black lines and labeled (e.g., Eruption 1 is labeled as E1). Daily estimates of volcanic noise are plotted above the colormap. Where volcanic noise is high, the calculated dv/v signal appears to become noisy. The mean cross-correlation empirical Green's function across the first 100 days is used as a template in calculating the dv/v . We do not include the final 50 days in our average, due to the high levels of volcanic noise. As we are calculating dv/v relative to an averaged signal over the first hundred days, spans of fiber which consistently increased in velocity over the period will show a negative dv/v for earlier days, and positive dv/v for later days.

3.2. Forward Modeling

We assume that to first-order, the observed dv/v signal is the result of volumetric strain associated with an opening dike, a reasonable choice given the dominance of dike opening over other volcanic processes in other studies of this volcanic intrusion and in analogous dv/v -based studies (Donaldson et al., 2019; Sigmundsson et al., 2024). Our study will invert for models of dike-opening, as opposed to inverting for the change in S velocity at varying location and depth and inferring dike geometries from that result. This choice allows us to more directly access parameters of interest, such as the depth and length of the dike, and in taking a Bayesian approach we may infer uncertainties on these quantities. Performing time-lapse tomography would also be relatively computationally expensive, in comparison, especially if we attempted to quantify uncertainties.

We forward model the expected dv/v from dike opening models defined by the center of the dike in map-view, at $[x_{cen}, y_{cen}]$, the azimuth of the dike θ , the depth extent of the dike, d_0 to d_1 , the length of the dike laterally, d_l , and the opening of the dike in meters A .

In general, rather than directly modeling dv/v , our analysis is placed in the framework of a change in arrival time (dt/t). In some instances, we discuss dt/t at points in space, in which case we are referring to a fractional change in traveltimes along infinitesimal segments at said points (also equal to the fractional change in slowness).

We may convert between dv/v and dt/t through the relation:

$$\frac{dt}{t} = \left(1 / \left(\frac{dv}{v} + 1 \right) \right) - 1 \quad (2)$$

Note that for $dt/t \ll 1$, $dt/t \approx -dv/v$.

Our inversion relies on forward modeling the expected dt/t signals between channel pairs for a chosen dike opening model. For said dike opening model, we consider an Okada model of dike opening (NIED, 2012; Okada, 1985), and predict the resulting volumetric strain in three-dimensional Cartesian space $\epsilon(x, y, z)$. At each point (x, y, z) , this strain may be mapped to a change in shear velocity dV_s/V_s through the empirical constant η :

$$\frac{dV_s}{V_s}(x, y, z) = -\eta \Delta\sigma(x, y, z) = -\eta K \epsilon(x, y, z), \quad (3)$$

where K is the bulk modulus (which we set to 50 GPa) and $\Delta\sigma$ is the stress perturbation associated with the dike-opening. This is a widely used scaling regularly employed in the literature (e.g., Donaldson et al., 2019; Niu et al., 2008; Sheng et al., 2022; Yamamura et al., 2003).

The value of η is expected to decay with increasing confining pressure, P (Daley et al., 2006). We assume that η takes the form of a power law:

$$\log_{10} \eta = -a \log_{10} P - b, \quad (4)$$

for P in MPa and η in Pa^{-1} , and constrain a and b through the results of laboratory experiments for consolidated rocks compiled by L. Li et al. (2023).

The value of a is reasonably consistent between experiments (1 ± 0.3), while b tends to vary heavily (7 ± 1.9) (L. Li et al., 2023). In our forward models, we use the mean values of a and b (1 and 7). The only model parameter affected by the high variability in b is the amplitude of dike opening—if η is underestimated by a factor of two, our inversion will overestimate dike opening by a factor of two—and we do not expect η to change between eruptions. Thus, we assume that all estimates of the log-amplitude of dike opening are biased by the same factor $\mathcal{E}(\eta_b)$, which is equal to the difference between the value of b used in our inversion and the true value of b .

From our dV_s/V_s estimates, we predict the change in Rayleigh wave slowness, $dt/t \approx -dv/v$, in a pointwise sense at varying period (i.e., at points in (x, y, T) space). The pointwise dt/t estimate is used to predict the change in arrival time for a source-receiver pair. Our approach to forward modeling is discussed in more depth in Text S3–S5 in Supporting Information S1, with a particular focus on the transitioning from dV_s/V_s to inter-channel dt/t .

3.3. Inversion

Using our estimates of pointwise dt/t and their uncertainty, we fit dike parameters through a Markov Chain Monte Carlo (MCMC) approach, implemented using the package emcee (Foreman-Mackey et al., 2012). Assuming uniform opening along a vertical, rectangular dike, we invert for the location, azimuth, and vertical extent of the structure.

We define an uncertainty structure for use in this inversion of the form:

$$\mathbf{C}_D = \mathbf{C}_d + \mathbf{C}_t \quad (5)$$

\mathbf{C}_d is a diagonal matrix imparting the uncertainty our of dt/t measurements. \mathbf{C}_t is a diagonal matrix associated with changes in the velocity which are not captured by our forward model (e.g., from atmospheric pressure, soil moisture, noise source variations, or volcanically driven stress changes which cannot be captured by our idealized dike) (Tarantola, 2005). We assume these variations are on the order of 0.5% (a similar variability to what is seen in e.g., Çubuk-Sabancı et al. (2024) or Maass et al. (2024), both of which are located on the Reykjanes peninsula), resulting in a matrix of the form $\mathbf{C}_t = (0.005)^2 \mathbf{I}$. We choose to use a diagonal uncertainty structure, down-sampling our data to reduce the effects of error covariance, as discussed above. Using a full covariance structure

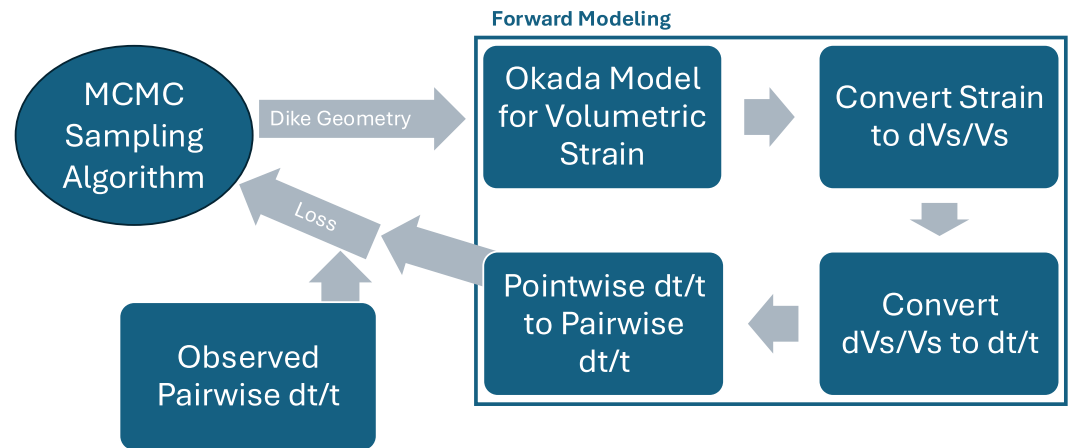


Figure 3. Flowchart summarizing forward modeling and inversion.

would be prohibitively time-consuming in our case, but might be possible in other contexts (e.g., given a more informative model prior which allows for faster convergence).

The probability of an individual model is then:

$$q(\mathbf{m}|\mathbf{d}) \propto e^{-\frac{1}{2}(\mathbf{G}(\mathbf{m})-\mathbf{d})^T \mathbf{C}_D(\mathbf{G}(\mathbf{m})-\mathbf{d})}, \quad (6)$$

where \mathbf{d} is the observed data, \mathbf{m} is a given dike-opening model, and \mathbf{G} maps said model to a data prediction. Here, we are assuming a uniform prior (i.e., $p(\mathbf{m}) \propto 1$). Our approach to analyzing dv/v signals is summarized in Figure 3.

4. Results

We plot the output distributions of dike opening models for eruption 1 (Figure 4, Figures S5–S7 in Supporting Information S1), eruption 2 (Figures S8–S11 in Supporting Information S1) and eruption 3 (Figure 5, Figures S12–S14 in Supporting Information S1). Alongside our distributions of dike opening models, we plot surface fissures associated with each eruption (LMI, 2024).

We find that our posterior distributions for eruptions 1 and 3 (E1 and E3) appear to impart real information regarding dike location, with a particularly excellent fit for E1. When plotted in map view, as in Figure 4, there is overlap between the posterior distribution and surface fissures associated with the eruption, suggesting that the location and azimuth of the dike are reasonably accurate (LMI, 2024). In both cases, the posterior distribution correctly indicates a dike which breaches the surface, and prefers dike-opening which is primarily located at shallow depths (less than 1 km). Our inversion of data from E1 predicts that $\log_{10}\text{opening} + \mathcal{E}(\eta_b) \approx 1$ (corresponding to 10 m), while the maximum dike opening in E1 predicted through geodetic measurements is approximately 4 m (Sigmundsson et al., 2024). This suggests $\mathcal{E}(\eta_b) \approx 0.5$ and $\log_{10} \eta \approx -\log_{10} P - 6.5$.

The third eruption is much less tightly constrained than the first eruption, likely due to a lower amplitude dv/v signal, which falls below noise along more of the array. The solution has two primary modes, with the likely location of the dike, as constrained by surface fissures, sitting on a the tail of the northwestern mode. The inversion of E3 also fails to provide a meaningful constraint on the length of the dike, a limitation which would likely be addressed if our array passed near both ends of the dike.

The inversion of data from eruption 2 arrives at a posterior distribution which is displaced from the volcanic fissures (LMI, 2024). Further, the preferred structure of E2 diverges from E1 and E3, with a greatly decreased dike opening over a dike with a much deeper extent, a result unsupported by Sigmundsson et al. (2024). The poor fit may be due in part to the fact that lava flows associated with this eruption extend much closer to the fiber than in the other eruptions. As such, our assumption that the dominant dv/v signal associated with the eruption is one of dike-opening may break down. Further, this dike appears to have propagated much closer to the fiber than the

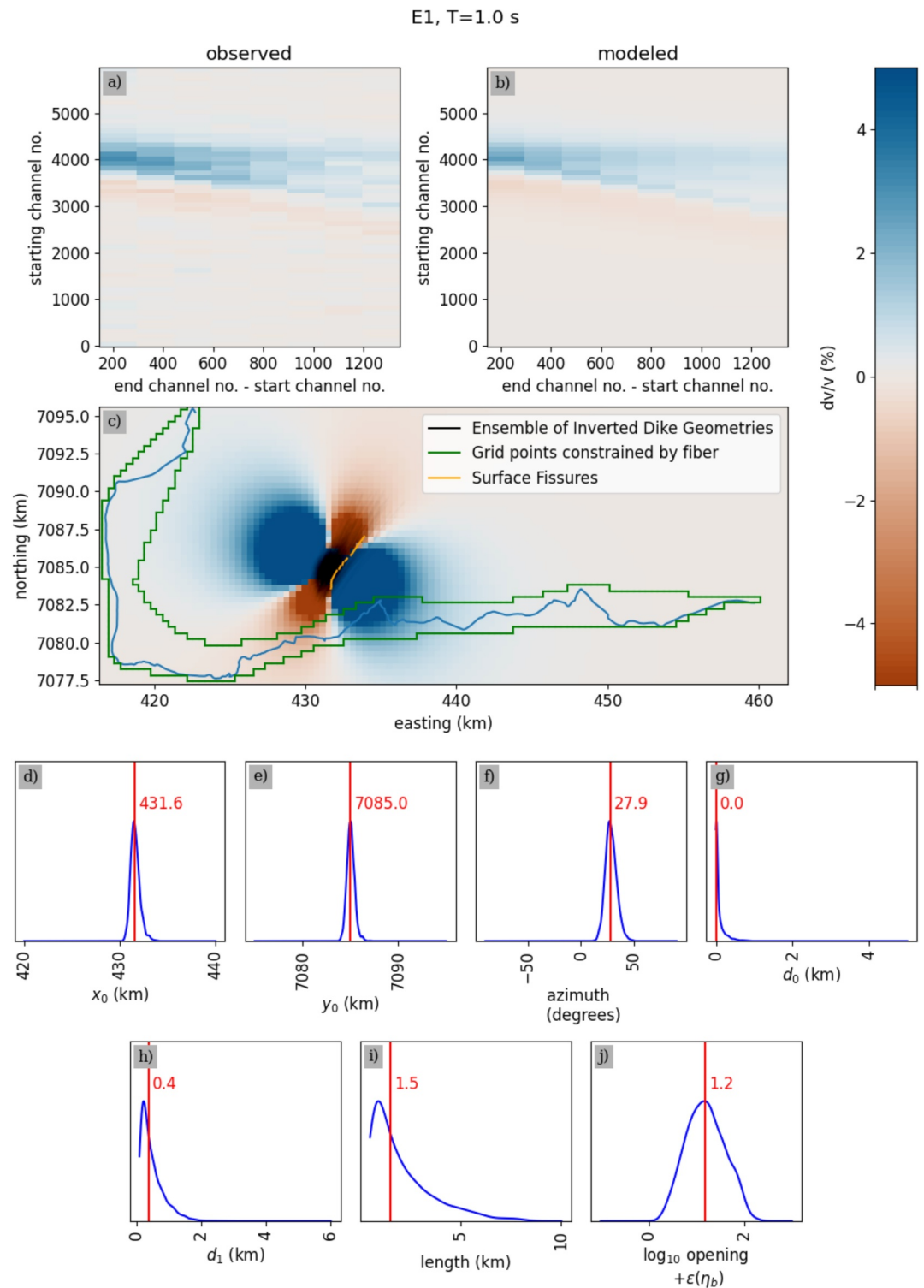


Figure 4. (a) Observed and (b) predicted dv/v signal during eruption 1 at a period of $T = 1$ s. Signals are smoothed on a 500 m lengthscale. The prediction is associated with the median solution from our MCMC inversion. (c) Map view of the predicted dv/v signal at a period of $T = 1$ s for the median output of our MCMC inversion. Inverted fiber channels are plotted in blue, with the green border outlining the grid points for which the dv/v signal is constrained for our data. Black lines are ensemble members from our inversion, signifying the location of dike opening, while orange lines denote observed surface fissures (LMI, 2024). (d)-(j) Posterior distributions for each dike opening parameter. Vertical axes of subplots show probability density normalized to the maximum probability for any given variable. Median values are marked in red.

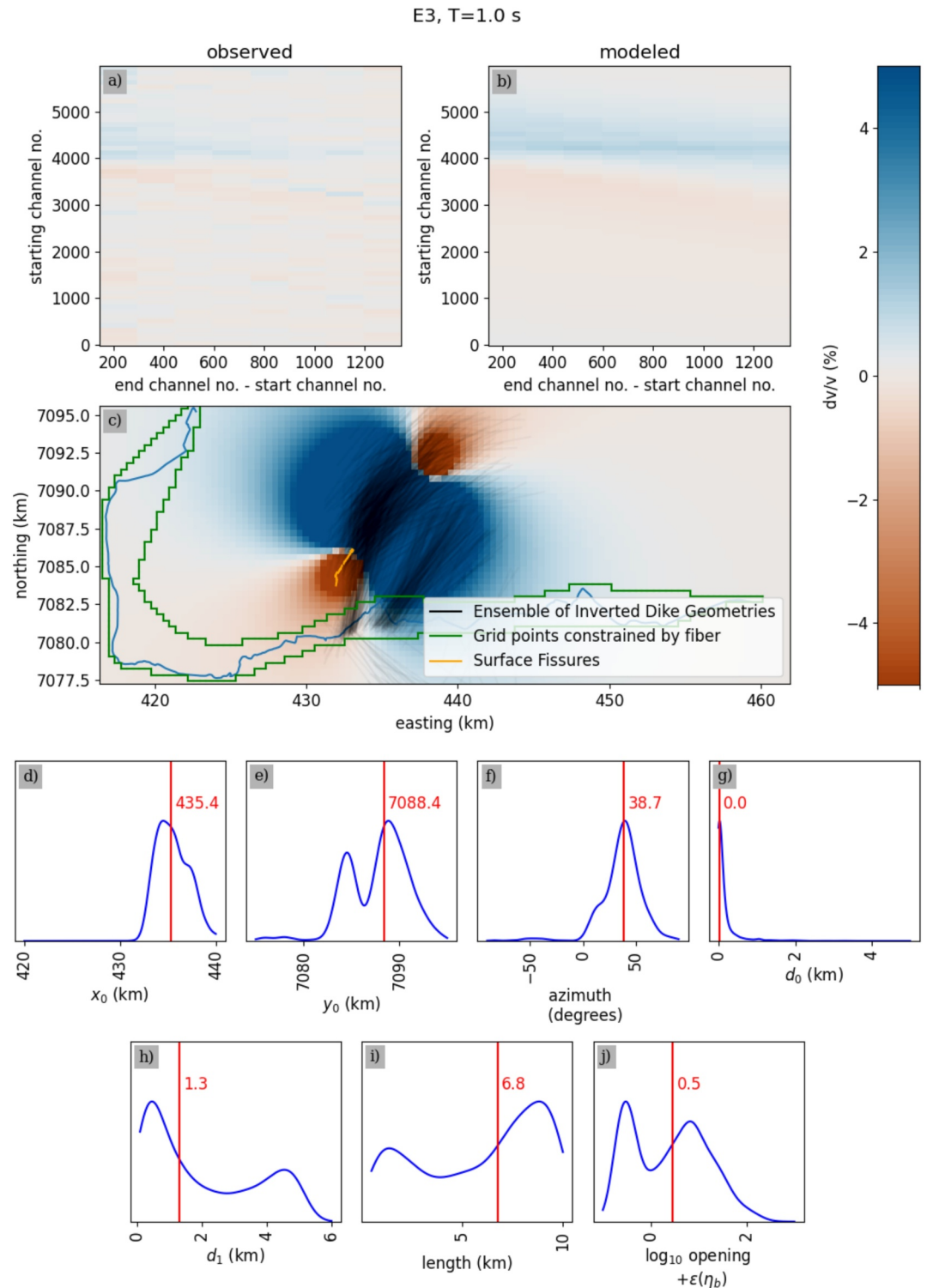


Figure 5. (a) Observed and (b) predicted dv/v signal during eruption 3 at a period of $T = 1$ s. Signals are smoothed on a 500 m lengthscale. The prediction is associated with the median solution from our MCMC inversion. (c) Map view of the predicted dv/v signal at a period of $T = 1$ s for the median output of our MCMC inversion. Inverted fiber channels are plotted in blue, with the green border outlining the grid points for which the dv/v signal is constrained for our data. Black lines are ensemble members from our inversion, signifying the location of dike opening, while orange lines denote observed surface fissures (LMI, 2024). (d)–(j) Posterior distributions for each dike opening parameter. Vertical axes of subplots show probability density normalized to the maximum probability for any given variable. Median values are marked in red.

others, potentially making our assumption of uniform deformation along a rectangular patch more problematic, as the local dike geometry may have dominated the dv/v signal along a span of the fiber.

5. Discussion

We have presented a new method of dv/v -based inference, inverting for an Okada model of dike-opening based solely on dv/v observation. Studies of volcanic dv/v initially focused on explaining changes in velocity structures over time through known changes in a volcanic system (or environmental signals), but with increasingly dense, high-quality data the field can move toward inferring volcanic dynamics, an exciting change in emphasis. Our approach is similar to that described in Sheng et al. (2022) which infers an Okada model associated with a slow-slip event on the basis of velocity changes, although we take an additional step in performing an inversion for our Okada model, aided by laboratory measurement of η . Likewise, a similar inversion to that presented in our study could naturally be applied to point sources in different volcanic contexts (Kiyoo, 1958).

The value of this kind of dv/v -based inversion is multi-fold. In some regions (e.g., in certain ocean-bottom contexts), seismic coverage might exceed what is available geodetically. Additionally, dv/v signals have been observed in the absence of geodetic signals (e.g., Mordret et al. (2010)). In such cases, the application of a dv/v -based inversion could illuminate volcanic structures which are otherwise inaccessible. Many common geodetic techniques also have drawbacks, some of which a dv/v -based seismic approach may avoid. For example, interferometric synthetic-aperture radar (InSAR) generally has low temporal resolution and may observe low coherence in areas of high vegetation (Fernández et al., 2017). Similarly, to achieve high spatial resolution in GNSS data one must average data over long timescales (Fernández et al., 2017).

Further, dv/v could be a powerful tool when used jointly with geodetic data. As surface waves of differing frequency have variable depth sensitivity, dv/v -based methods will sample deformation in a different way than approaches such as InSAR or global navigation satellite systems (GNSS), which describe surface deformation (Fernández et al., 2017). Comprehensively considering dv/v signals in different frequency bands may provide us with stronger constraints on volcanic features. Our study, in particular, provides a distribution of potential dike depth extents, which may be considered in concert with geometries derived geodetically to better capture the shape of the feature. In localizing a velocity change within a range of depths, we generally require that data at multiple frequency bands have sensitivity in that depth range. In our case, sensitivity kernels indicate that we will likely fail to localize the depth of any velocity changes deeper than 3 km.

Appreciating the great potential of increasingly quantitative applications of dv/v , it is also critical that we recognize the simplifications which may limit the broad applicability of the inversion we have presented. Okada models assume elastic deformation to a homogeneous half-space, a simplification to the composition and deformation of the study region. Further, our Okada model assumes uniform dike opening along a single rectangular section. This parameterization is an idealization of the true dike geometry, intended to provide first-order information about its depth and location relative to the fiber, but its simplicity may result in some of the misfit between prediction and observation. For example, dikes often observe increased opening closer to the free surface and see variable opening along-strike, and thus a uniform opening in depth is expected to be non-physical (Geshi et al., 2020; Sigmundsson et al., 2015). The effect of this simplification can be clearly observed when our results are compared with other observations. The median lateral length of the first dike-opening event from our posterior distribution is 1.5 km, while surface fissures extend closer to 5 km, likely due to variable degrees opening along the fissures (LMI, 2024). Likewise, the results of Sigmundsson et al. (2024) suggest that dike-opening during the first eruption extended deeper and further laterally than our observation. However, the study suggested that the maximum opening occurred in a patch with a length of ≈ 1 km and depth of ≈ 0.5 km, which agrees well with our inversion.

Additionally, while we are able to forward model volumetric strain to dVs/Vs through laboratory measurements, the scaling between these quantities, η , can vary greatly depending on material (L. Li et al., 2023). While outside the scope of this study, future inversions could calibrate the relationship between these quantities based on known strain signals at the site (e.g., those observed geodetically). In certain contexts, no ground-truth deformation signal is available, so our choice to fit models without calibration of η allows for a more general understanding of the power of dv/v -based inversions.

We also assume a constant velocity model (and thus make a straight-ray approximation). In reality, lateral heterogeneities in the starting velocity model will impact how the stress from dike opening is propagated to a dv/v between channel pairs, as the forward propagation of depth-dependent dV_s/V_s to dv/v is tied to the starting Versus model. Further, when integrating pointwise dt/t to get dt/t along a raypath, the weight of any given point will scale with its absolute Rayleigh velocity. In the case of extreme velocity gradients, the raypaths may experience non-negligible bending, a further complication to the forward problem.

Finally, we treat all dv/v signals unrelated to dike opening as noise. Future work could instead forward model dv/v associated with known environmental factors, such as temperature and rainfall, and use the result as a correction. This could be of particular value in accounting for dv/v from other reservoirs in the volcanic system, such as dike-feeding magma chambers, co-eruptive faulting, tremor-related noise source variations, or lava flows at the surface, as these signals are likely to have significant covariance with that of an opening dike.

6. Conclusion

As we move toward an age of increased, dense seismic instrumentation, studies of temporal seismic velocity change are increasingly well-constrained. We observed changes in Rayleigh wave phase velocity on the order of 2% associated with the 2023–2024 eruptions on the Reykjanes peninsula. We explain some of these signals through simple models of uniform dike opening along a vertical, rectangular patch. Said models of dike opening are consistent with the location of surface fissures.

Our result has implications both for the study of volcanic systems and generally for the use of dv/v as a measure of stress change. Moving forward, we hope to build on the methodology employed here and apply it in varied settings throughout the Earth system.

Conflict of Interest

The authors declare no conflicts of interest relevant to this study.

Data Availability Statement

Data are available on CaltechDATA (Bird & Zhan, 2024).

References

- Ajo-Franklin, J. B., Dou, S., Lindsey, N. J., Monga, I., Tracy, C., Robertson, M., et al. (2019). Distributed acoustic sensing using dark fiber for near-surface characterization and broadband seismic event detection. *Scientific Reports*, 9(1), 1328. <https://doi.org/10.1038/s41598-018-36675-8>
- Atterholt, J., Zhan, Z., Yang, Y., & Zhu, W. (2024). Imaging the garlock fault zone with a fiber: A limited damage zone and hidden bimaterial contrast. *Journal of Geophysical Research: Solid Earth*, 129(7), e2024JB028900. <https://doi.org/10.1029/2024JB028900>
- Biondi, E., Wang, X., Williams, E. F., & Zhan, Z. (2022). Geolocalization of large-scale DAS channels using a GPS-tracked moving vehicle. *Seismological Research Letters*, 94(1), 318–330. <https://doi.org/10.1785/0220220169>
- Biondi, E., Zhu, W., Li, J., Williams, E. F., & Zhan, Z. (2023). An upper-crust lid over the Long Valley magma chamber. *Science Advances*, 9(42), eadi9878. <https://doi.org/10.1126/sciadv.adi9878>
- Bird, E., & Zhan, Z. (2024). Ambient Noise Cross-Correlation Data associated with “Constraining Dike Opening Models With Seismic Velocity Changes Associated with the 2023–2024 Eruption Sequence on the Reykjanes Peninsula” by Bird et al [Dataset]. *CaltechDATA*. <https://doi.org/10.22002/kxtar-bm759>
- Brenguier, F., Shapiro, N. M., Campillo, M., Ferrazzini, V., Duputel, Z., Coutant, O., & Nercessian, A. (2008). Towards forecasting volcanic eruptions using seismic noise. *Nature Geoscience*, 1(2), 126–130. <https://doi.org/10.1038/ngeo104>
- Campillo, M., & Paul, A. (2003). Long-range correlations in the diffuse seismic coda. *Science*, 299(5606), 547–549. <https://doi.org/10.1126/science.1078551>
- Caudron, C., Miao, Y., Spica, Z. J., Wollin, C., Haberland, C., Jousset, P., et al. (2024). Monitoring underwater volcano degassing using fiber-optic sensing. *Scientific Reports*, 14(1), 3128. <https://doi.org/10.1038/s41598-024-53444-y>
- Cheng, F., Ajo-Franklin, J. B., & Rodriguez Tribaldos, V. (2023). High-resolution near-surface imaging at the basin scale using dark fiber and distributed acoustic sensing: Toward site effect estimation in urban environments. *Journal of Geophysical Research: Solid Earth*, 128(9), e2023JB026957. <https://doi.org/10.1029/2023JB026957>
- Clements, T., & Denolle, M. A. (2018). Tracking groundwater levels using the ambient seismic field. *Geophysical Research Letters*, 45(13), 6459–6465. <https://doi.org/10.1029/2018GL077706>
- Çubuk-Sabuncu, Y., Jónsdóttir, K., Árnadóttir, T., Mordret, A., Caudron, C., Lecocq, T., & De Plaen, R. (2024). Temporal seismic velocity changes associated with the Mw 6.1, May 2008 Ölfus Doublet, South Iceland: A joint interpretation from dv/v and GPS. *Journal of Geophysical Research: Solid Earth*, 129(4), e2023JB027064. <https://doi.org/10.1029/2023JB027064>
- Daley, T. M., Schoenberg, M. A., Rutqvist, J., & Nihei, K. T. (2006). Fractured reservoirs: An analysis of coupled elastodynamic and permeability changes from pore-pressure variation. *Geophysics*, 71(5), O33–O41. <https://doi.org/10.1190/1.2231108>

Acknowledgments

This work was supported by the Gordon and Betty Moore Foundation, the National Science Foundation (NSF) Center for Geomechanics and Mitigation of Geohazards (1822214), and the NSF Faculty Early Career Development Program (CAREER), award number 1848166. Our work was guided by valuable conversations with Robert Clayton, Michael Gurnis, Tobias Koehne, Yuan-Kai Liu, Auden Reid-McLaughlin, Alba Rodríguez Padilla, John Wilding, and Shane Zhang. We thank those involved in the review process for this work, including Marcos Moreno (editor), John Browning (reviewer), and two anonymous reviewers.

- Donaldson, C., Caudron, C., Green, R. G., Thelen, W. A., & White, R. S. (2017). Relative seismic velocity variations correlate with deformation at Kīlauea Volcano. *Science Advances*, 3(6), e1700219. <https://doi.org/10.1126/sciadv.1700219>
- Donaldson, C., Winder, T., Caudron, C., & White, R. S. (2019). Crustal seismic velocity responds to a magmatic intrusion and seasonal loading in Iceland's Northern Volcanic Zone. *Science Advances*, 5(11), eaax6642. <https://doi.org/10.1126/sciadv.aax6642>
- Fernández, J., Pepe, A., Poland, M. P., & Sigmundsson, F. (2017). Volcano Geodesy: Recent developments and future challenges. *Journal of Volcanology and Geothermal Research*, 344, 1–12. <https://doi.org/10.1016/j.jvolgeores.2017.08.006>
- Foreman-Mackey, D., Hogg, D. W., Lang, D., & Goodman, J. (2012). Emcee: The MCMC Hammer. *Publications of the Astronomical Society of the Pacific*, 125(925), 306–312. <https://doi.org/10.1086/670067>
- Geshi, N., Browning, J., & Kusumoto, S. (2020). Magmatic overpressures, volatile exsolution and potential explosivity of fissure eruptions inferred via dike aspect ratios. *Scientific Reports*, 10(1), 9406. <https://doi.org/10.1038/s41598-020-66226-z>
- Jousset, P., Currenti, G., Schwarz, B., Chalari, A., Tilmann, F., Reinsch, T., et al. (2022). Fibre optic distributed acoustic sensing of volcanic events. *Nature Communications*, 13(1), 1753. <https://doi.org/10.1038/s41467-022-29184-w>
- Kiyoo, M. (1958). Relations between the eruptions of various volcanoes and the deformations of the ground surfaces around them. *Earthq Res Inst*, 36, 99–134.
- Klaasen, S., Thrastarson, S., Çubuk-Sabuncu, Y., Jónsdóttir, K., Gebraad, L., Paiz, P., & Fichtner, A. (2023). Subglacial volcano monitoring with fibre-optic sensing: Grímsvötn, Iceland. *Volcanica*, 6(2), 301–311. <https://doi.org/10.30909/vol.06.02.301311>
- Li, J., Kim, T., Lapusta, N., Biondi, E., & Zhan, Z. (2023a). The break of earthquake asperities imaged by distributed acoustic sensing. *Nature*, 620(7975), 800–806. <https://doi.org/10.1038/s41586-023-06227-w>
- Li, L., Li, J., & Song, X. (2023b). Temporal variations in low-frequency Rayleigh-wave velocities should mostly originate from the shallow crust. <https://doi.org/10.13140/RG.2.2.11079.27045/1>
- Lindsey, N. J., Dawe, T. C., & Ajo-Franklin, J. B. (2019). Illuminating seafloor faults and ocean dynamics with dark fiber distributed acoustic sensing. *Science*, 366(6469), 1103–1107. <https://doi.org/10.1126/science.aay5881>
- LMI. (2024). Landmælingar Íslands [Dataset]. (data collected by the Icelandic institute of natural history and the national survey of Iceland).
- Ma, Y., Ajo-Franklin, J., Nayak, A., Zhu, X., & Correa, J. (2023). DAS microseismic reflection imaging for hydraulic fracture and fault zone mapping. In *Third international meeting for applied geoscience and energy expanded abstracts* (pp. 459–463). Society of Exploration Geophysicists and American Association of Petroleum Geologists. <https://doi.org/10.1190/image2023-3907834.1>
- Maass, R., Schippkus, S., Hadziioannou, C., Schwarz, B., Jousset, P., & Krawczyk, C. (2024). Stacking of distributed dynamic strain reveals link between seismic velocity changes and the 2020 unrest in Reykjanes. *Journal of Geophysical Research: Solid Earth*, 129(6), e2023JB028320. <https://doi.org/10.1029/2023JB028320>
- Málek, J., Brokešová, J., & Novotný, O. (2019). Seismic structure beneath the Reykjanes Peninsula, southwest Iceland, inferred from array-derived Rayleigh wave dispersion. *Tectonophysics*, 753, 1–14. <https://doi.org/10.1016/j.tecto.2018.12.020>
- Martuganova, E., Stiller, M., Norden, B., Hennings, J., & Krawczyk, C. M. (2022). 3D deep geothermal reservoir imaging with wireline distributed acoustic sensing in two boreholes. *Solid Earth*, 13(8), 1291–1307. <https://doi.org/10.5194/se-13-1291-2022>
- Mata Flores, D., Mercerat, E. D., Ampuero, J. P., Rivet, D., & Sladen, A. (2023). Identification of two vibration regimes of underwater fibre optic cables by distributed acoustic sensing. *Geophysical Journal International*, 234(2), 1389–1400. <https://doi.org/10.1093/gji/ggad139>
- Mordret, A., Jolly, A. D., Duputel, Z., & Fournier, N. (2010). Monitoring of phreatic eruptions using interferometry on retrieved cross-correlation function from ambient seismic noise: Results from Mt. Ruapehu, New Zealand. *Journal of Volcanology and Geothermal Research*, 191(1), 46–59. <https://doi.org/10.1016/j.jvolgeores.2010.01.010>
- NIED, N. R. I. F. E. S. A. D. R. (2012). Program to calculate deformation due to a fault model DC3D0/DC3D [Software]. <https://www.bosai.go.jp/e/dc3d.html>
- Niu, F., Silver, P. G., Daley, T. M., Cheng, X., & Majer, E. L. (2008). Preseismic velocity changes observed from active source monitoring at the Parkfield SAFOD drill site. *Nature*, 454(7201), 204–208. <https://doi.org/10.1038/nature07111>
- Okada, Y. (1985). Surface deformation due to shear and tensile faults in a half-space. *Bulletin of the Seismological Society of America*, 75(4), 1135–1154. <https://doi.org/10.1785/BSSA0750041135>
- Parks, M., Sigmundsson, F., Barsotti, S., Geirsson, H., Vogfjörð, K. S., Ófeigsson, B. G., & Einarsson, P. (2024). Volcano-Tectonic activity on the Reykjanes peninsula since 2019: Overview and associated hazards IReykjanes peninsula. <https://en.vedur.is/volcanoes/fagradalsfjall-eruption/>
- Rodríguez Tribaldos, V., & Ajo-Franklin, J. B. (2021). Aquifer monitoring using ambient seismic noise recorded with distributed acoustic sensing (DAS) deployed on dark fiber. *Journal of Geophysical Research: Solid Earth*, 126(4), e2020JB021004. <https://doi.org/10.1029/2020JB021004>
- Sens-Schönfelder, C., Pomponi, E., & Peltier, A. (2014). Dynamics of Piton de la Fournaise volcano observed by passive image interferometry with multiple references. *Journal of Volcanology and Geothermal Research*, 276, 32–45. <https://doi.org/10.1016/j.jvolgeores.2014.02.012>
- Sens-Schönfelder, C., & Wegler, U. (2006). Passive image interferometry and seasonal variations of seismic velocities at Merapi Volcano, Indonesia. *Geophysical Research Letters*, 33(21), L21302. <https://doi.org/10.1029/2006GL027797>
- Shen, Z., Yang, Y., Fu, X., Adams, K. H., Biondi, E., & Zhan, Z. (2024). Fiber-optic seismic sensing of vadose zone soil moisture dynamics. *Nature Communications*, 15(1), 6432. <https://doi.org/10.1038/s41467-024-50690-6>
- Sheng, Y., Mordret, A., Sager, K., Brenguier, F., Boué, P., Rousset, B., et al. (2022). Monitoring seismic velocity changes across the San Jacinto fault using train-generated seismic tremors. *Geophysical Research Letters*, 49(19), e2022GL098509. <https://doi.org/10.1029/2022GL098509>
- Sigmundsson, F., Hooper, A., Hreinsdóttir, S., Vogfjörð, K. S., Ófeigsson, B. G., Heimisson, E. R., et al. (2015). Segmented lateral dyke growth in a rifting event at Bárðarbunga volcanic system, Iceland. *Nature*, 517(7533), 191–195. <https://doi.org/10.1038/nature14111>
- Sigmundsson, F., Parks, M., Geirsson, H., Hooper, A., Drouin, V., Vogfjörð, K. S., & Barsotti, S. (2024). Fracturing and tectonic stress drives ultrarapid magma flow into dikes. *Science*, 383(6688), eadn2838. <https://doi.org/10.1126/science.adn2838>
- Sladen, A., Rivet, D., Ampuero, J. P., De Barros, L., Hello, Y., Calbris, G., & Lamare, P. (2019). Distributed sensing of earthquakes and ocean-solid Earth interactions on seafloor telecom cables. *Nature Communications*, 10(1), 5777. <https://doi.org/10.1038/s41467-019-13793-z>
- Tarantola, A. (2005). *Inverse problem theory and methods for model parameter estimation*. Society for Industrial and Applied Mathematics. <https://doi.org/10.1137/1.9780898717921>
- Wegler, U., & Sens-Schönfelder, C. (2007). Fault zone monitoring with passive image interferometry. *Geophysical Journal International*, 168(3), 1029–1033. <https://doi.org/10.1111/j.1365-246X.2006.03284.x>
- Williams, E. F., Fernández-Ruiz, M. R., Magalhaes, R., Vanthillo, R., Zhan, Z., González-Herráez, M., & Martins, H. F. (2019). Distributed sensing of microseisms and teleseisms with submarine dark fibers. *Nature Communications*, 10(1), 5778. <https://doi.org/10.1038/s41467-019-13262-7>
- Williams, E. F., Ugalde, A., Martins, H. F., Becerril, C. E., Callies, J., Claret, M., et al. (2023). Fiber-optic observations of internal waves and tides. *Journal of Geophysical Research: Oceans*, 128(9), e2023JC019980. <https://doi.org/10.1029/2023JC019980>

- Yamamura, K., Sano, O., Utada, H., Takei, Y., Nakao, S., & Fukao, Y. (2003). Long-term observation of in situ seismic velocity and attenuation. *Journal of Geophysical Research*, *108*(B6), 2002JB002005. <https://doi.org/10.1029/2002JB002005>
- Yang, Y., Atterholt, J. W., Shen, Z., Muir, J. B., Williams, E. F., & Zhan, Z. (2022). Sub-kilometer correlation between near-surface structure and ground motion measured with distributed acoustic sensing. *Geophysical Research Letters*, *49*(1), e2021GL096503. <https://doi.org/10.1029/2021GL096503>
- Zhan, Z. (2020). Distributed acoustic sensing turns fiber-optic cables into sensitive seismic antennas. *Seismological Research Letters*, *91*(1), 1–15. <https://doi.org/10.1785/0220190112>
- Zhan, Z., Tsai, V. C., & Clayton, R. W. (2013). Spurious velocity changes caused by temporal variations in ambient noise frequency content. *Geophysical Journal International*, *194*(3), 1574–1581. <https://doi.org/10.1093/gji/ggt170>

References From the Supporting Information

- Field, E. H., Jacob, K. H., & Hough, S. E. (1992). Earthquake site response estimation: A weak-motion case study. *Bulletin of the Seismological Society of America*, *82*(6), 2283–2307. <https://doi.org/10.1785/BSSA0820062283>
- Herrmann, R. B. (2013). Computer programs in seismology: An evolving tool for instruction and research. *Seismological Research Letters*, *84*(6), 1081–1088. <https://doi.org/10.1785/0220110096>
- Shearer, P. M., Prieto, G. A., & Hauksson, E. (2006). Comprehensive analysis of earthquake source spectra in southern California. *Journal of Geophysical Research*, *111*(B6), B06303. <https://doi.org/10.1029/2005JB003979>